International Journal of Multiphase Flow 58 (2014) 139–153

Contents lists available at ScienceDirect

International Journal of Multiphase Flow

journal homepage: www.elsevier.com/locate/ijmulflow

Triple decomposition technique in air–water flows: Application to instationary flows on a stepped spillway

Stefan Felder, Hubert Chanson *

The University of Queensland, School of Civil Engineering, Brisbane, QLD 4072, Australia

ARTICLE INFO

Article history:
Received 22 January 2013
Received in revised form 24 July 2013
Accepted 12 September 2013
Available online 20 September 2013

Keywords:
Instationary air–water flows
Flow instabilities
Turbulence
Phase-detection probe
Signal processing
Triple decomposition
Pooled stepped spillway

ABSTRACT

Self-sustained instabilities and pseudo-periodic motion may be observed in hydraulic structures and industrial flows. Documented examples include the hydraulic jump, sloshing motion in a reservoir and surging waves in pooled stepped spillways. The instabilities may generate some very large turbulence levels and integral turbulent scales, combining the contributions of both slow fluctuations and fast turbulent fluctuations. Herein a triple decomposition of phase-detection probe signals was developed to identify the turbulent contributions of the slow and fast velocity components in highly aerated free-surface flows. The raw probe signals were split into slow and fast signal components and the air–water flow properties of each component were calculated. The method was applied to a new data set collected down a stepped spillway channel with two stepped configurations (flat and pooled). The latter configuration experienced some self-sustained pseudo-periodic instabilities. The data analysis results showed that the fast turbulent velocity fluctuations of the decomposed signal were close to the turbulence levels on the flat stepped spillway (i.e. in absence of instability). And the largest turbulent energy was contained in the slow fluctuating velocity component. The findings showed a new implementation of a triple decomposition technique to instationary air–water flows.

1. Introduction

In the past decades, many studies investigated experimentally air–water flows with natural free-surface aeration, including free-surface flows down spillway chutes (Rao and Kobus, 1971; Wood, 1991; Chanson, 2013). Most experimental works of air–water flows focused upon the time-averaged air–water flow properties providing basic flow information for the design of hydraulic structures (Wood, 1991; Chanson, 1997). Self-sustained instabilities and pseudo-periodic motion may be observed in air–water flows in hydraulic structures and industrial flows. Documented examples include the hydraulic jump (Bradley and Peterka, 1957; Mossa, 1999), sloshing motion in a reservoir (Armenio and La Rocca, 1996) and jump waves in pooled stepped spillways (Chanson, 2001; Thorwarth, 2008). Fig. 1 illustrates two prototype applications.

The appearance of instability processes depends on the flow conditions and configurations including boundary conditions. A number of researchers documented the unsteady nature of the air–water flows and associated surface waves (Killen, 1968; Toombes and Chanson, 2007). Mossa and Tolve (1998) and Leandro et al. (2012) studied the hydraulic jump fluctuations and their impact on void fraction distribution and free-surface profile. Toombes and Chanson (2007) showed the effect of surface waves on the void fraction and bubble count rates. On flat stepped spillways, some flow instabilities were observed for some intermediate flow rates (Elviro and Mateos, 1995; Chanson, 1996; Ohtsu and Yasuda, 1997). In pooled stepped chutes, some pseudo-periodic flow was documented on the Sorpe dam spillway during some uncontrolled spillway release (Chanson, 2001) and physically investigated by Thorwarth and Koengeter (2006) and Thorwarth (2008). The self-sustained unstable processes appeared at the spillway's upstream end and the jump waves propagated downstream (Fig. 1A).

Herein new experiments were conducted in a stepped chute with two stepped configurations: flat steps and pooled steps. Flow instabilities were observed in the latter setup and a new triple decomposition technique is introduced for the analysis of phase detection probe signals including the velocity fluctuation estimates, taking into account both the fast turbulent and slow fluctuating velocity components. After a short description of the physical setup, some basic observations are shown, before the triple decomposition technique is applied.

2. Signal processing of phase detection intrusive probes

2.1. Basic signal processing

In a free-surface flow, the void fraction ranges typically from 0% to 100%, as illustrated in Fig. 1A, and the mass and momentum

* Corresponding author.
E-mail address: h.chanson@uq.edu.au (H. Chanson).

0301-9322/$ - see front matter © 2013 Elsevier Ltd. All rights reserved.
http://dx.doi.org/10.1016/j.ijmultiphaseflow.2013.09.006

Fig. 1. Surge instabilities in high-velocity open channel flows (A) free-surface instability down the Sorpe dam spillway, Germany in 2003 (Courtesy of Ruhrverband) – θ = 18°, h 0 0.5–2 m (pooled steps), Q = 6.9 m^3/s, Re = 1 × 10^6 and (B) air–water-sediment surges down a channelised section of Rio Achumani, La Paz, Bolivia in 1993 (Courtesy of Francis Fruchard) – Flat step design.

fluxes are encompassed within the flow region with void fractions less than 95% (Cain, 1978; Wood, 1985). A number of physical data demonstrated that the high-velocity gas–liquid flows behave as a quasi-homogenous mixture and the two phases travel with a nearly identical velocity, the slip velocity being negligible (Rao and Kobus, 1971; Cain and Wood, 1981; Wood, 1991; Chanson, 1997). In such aerated flows, a robust metrology is the phase-detection needle probe (Fig. 2A). Although the first needle probe designs were based upon resistivity probes, both optical fibre and resistivity probe systems are commonly used (Cartellier, 1992; Chanson, 2002). The needle probe is designed to pierce bubbles and droplets. Fig. 2B illustrates a typical signal output and corresponding instantaneous void fraction. The flow conditions are listed in the figure caption. In Fig. 2B, each steep drop of the signal corresponds to an air bubble pierced by the probe tip.

In free-surface flows, the basic signal processing of the raw voltage signals is based upon a single threshold technique and some statistical analyses of the raw signal. The threshold is typically between 40% and 50% of the air–water range (Toombes, 2002; Chanson and Felder, 2010). The basic outputs are the void fraction, the bubble count rate and air/water chord size distributions.

A cross-correlation analysis between the two probe tip signals yields the maximum cross-correlation $(R_{xy})_{max}$ for a time lag T corresponding to the average interfacial travel time between the probe sensors (Herringe and Davis, 1976; Chanson, 1997). The time-averaged interfacial velocity V is calculated as $V = \Delta x/T$ where Δx is the distance between probe sensors. The integration of the auto- and cross-correlation functions from the maximum correlation $(R_{xy})_{max}$ to the first zero-crossing yields the correlation integral time scales T_{xx} and T_{xy} (Fig. 2C):

$$T_{xx} = \int_{\tau=0}^{\tau=\tau(R_{xx}=0)} R_{xx}(\tau) \times d\tau \quad (1)$$

$$T_{xy} = \int_{\tau=\tau(R_{xy}=(R_{xy})_{max})}^{\tau=\tau(R_{xy}=0)} R_{xy}(\tau) \times d\tau \quad (2)$$

where T_{xx} is the auto-correlation integral time scale characterising the longitudinal air–water flow structure and the cross-correlation integral time scale T_{xy} characterises the vortices advecting the air–water flow structure (Chanson and Carosi, 2007). The broadening of the cross-correlation function compared to the auto-correlation function yields the turbulence intensity (Kipphan, 1977; Chanson and Toombes, 2002). The dimensionless expression of the turbulence velocity fluctuations may be expressed as (Appendix A):

$$Tu = \frac{\sqrt{2}}{\sqrt{\pi} \times T} \times \sqrt{\left(\frac{T_{xy}}{(R_{xy})_{max}}\right)^2 - T_{xx}^2} \quad (3)$$

where T_{xy} and T_{xx} are the correlation time scales (Eqs. (1), (2)) (Fig. 2C). Within some approximations (Appendix A), a simplified result is (Chanson and Toombes, 2002):

$$Tu = 0.851 \times \sqrt{\frac{\tau_{0.5}^2 - T_{0.5}^2}{T}} \quad (4)$$

where $\tau_{0.5}$ is the time scale for which $R_{xy}(T + \tau_{0.5}) = 0.5 \times R_{xy}(T)$, and $T_{0.5}$ is the characteristic time for which $R_{xx}(T_{0.5}) = 0.5$.

2.2. Signal decomposition technique

When a monophase flow motion is characterised by slow fluctuations, a turbulence characterisation may be based upon a triple decomposition of the instantaneous velocity signal (e.g. Hussain and Reynolds, 1972; Lyn and Rodi, 1994; Fox et al., 2005; Brown and Chanson, 2013). The instantaneous velocity signal $u(t)$ is decomposed into three components:

$$u(t) = U + u'(t) + u''(t) \quad (5)$$

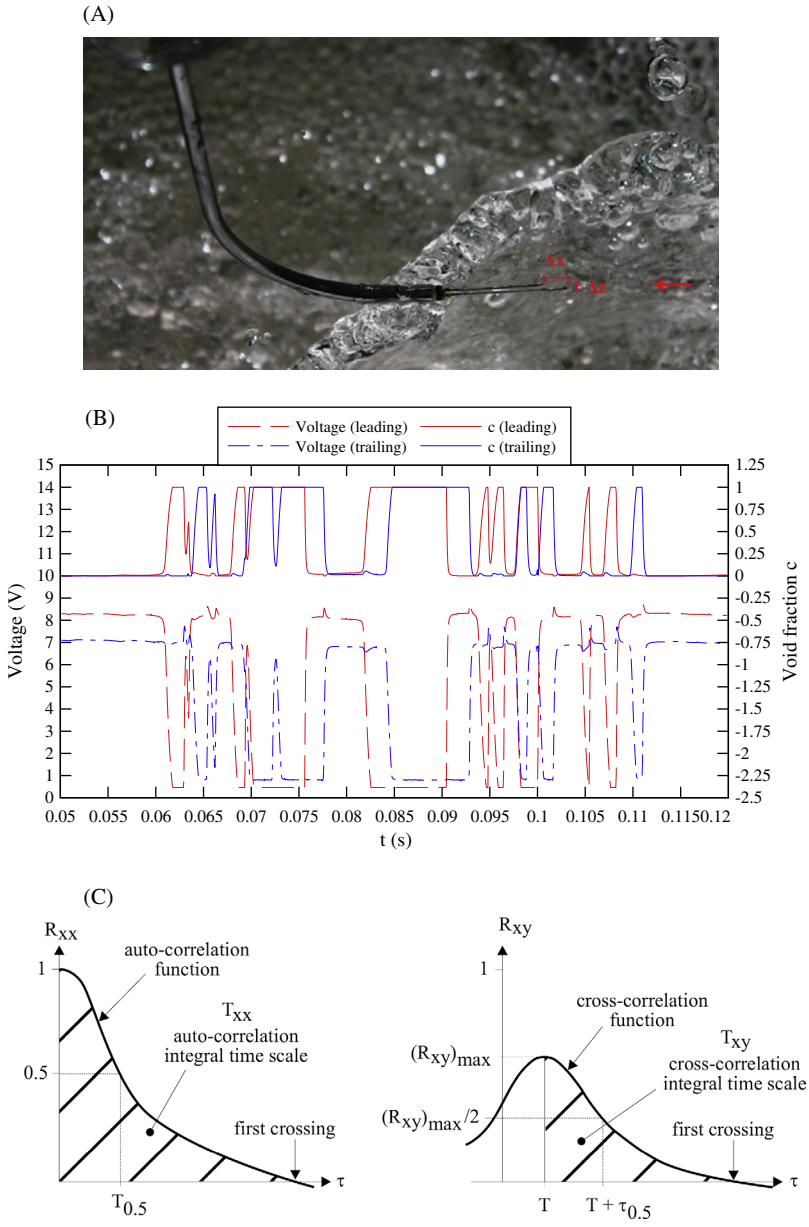

Fig. 2. Phase detection intrusive probe and signal output, (A) double-tip conductivity probe (Ø = 0.13 mm) – Probe aligned parallel to main flow direction (flow from right to left), (B) double-tip probe voltage output and corresponding instantaneous void fraction: q_w = 0.152 m^2/s, y = 0.072 m, C = 0.20, F = 58 Hz, V = 3.1 m/s, Re = 6.0 × 10^5, step edge, Pooled step edge 18, (C) definition sketch of auto- and cross-correlation functions.

where U is a mean velocity component, $u'(t)$ represents the slow fluctuating velocity and $u''(t)$ the fast fluctuating velocity component which corresponds to the 'true' turbulent motion. With a phase-detection intrusive probe, the interfacial velocity signal is not continuous. Herein a triple decomposition method was applied to the raw probe signals of a double-tip phase detection probe. Both signals were split into three components reflecting the mean, slow fluctuating and fast fluctuating contributions (Fig. 3). The approach was similar to the mono-phase flow technique, but applied to the phase-detection probe signal rather than to the velocity signal.

2.2.1. Characteristic frequencies and signal decomposition

The raw signal decomposition was performed using some characteristic cut-off frequencies which were identified using visual observations as well as power spectra analyses of raw signals. In the present study, self-sustained instabilities were observed with typical frequencies within the range of 0.5–2 Hz during laboratory experiments performed on a pooled stepped chute. These were also seen in the spectral analyses of the probe signals (Fig. 4). Fig. 4A shows some typical power spectra of probe voltage signal, together with a smoothed curve, highlighting some peaks and troughs in the power spectrum density functions within 0.3–2 Hz (e.g. 1.87 Hz in Fig. 4A). Some characteristic frequencies of about 0.3–0.8 Hz were also observed in the power spectrum of interfacial velocities, calculated by correlation analyses for short time periods of 0.1 s (10 Hz) (Fig. 4B). For example, some higher power spectrum density function levels are seen in Fig. 4B for frequencies between 0.3 and 0.7 Hz, while Fig. 5 illustrates a typical time-series of interfacial velocity calculated using cross-correlation analyses for 0.1 s periods. For the present data set, a sensitivity analysis was performed in terms of the cut-off frequencies and the results yielded a meaningful lower cut-off frequency of 0.33 Hz and an upper cut-off frequency of 10 Hz. Thereafter the mean signal was the low pass filtered component with a cut-off frequency of 0.33 Hz, and the slow fluctuating signal was a band pass filtered component with upper and lower cut-off frequencies of 10 Hz and 0.33 Hz respectively.

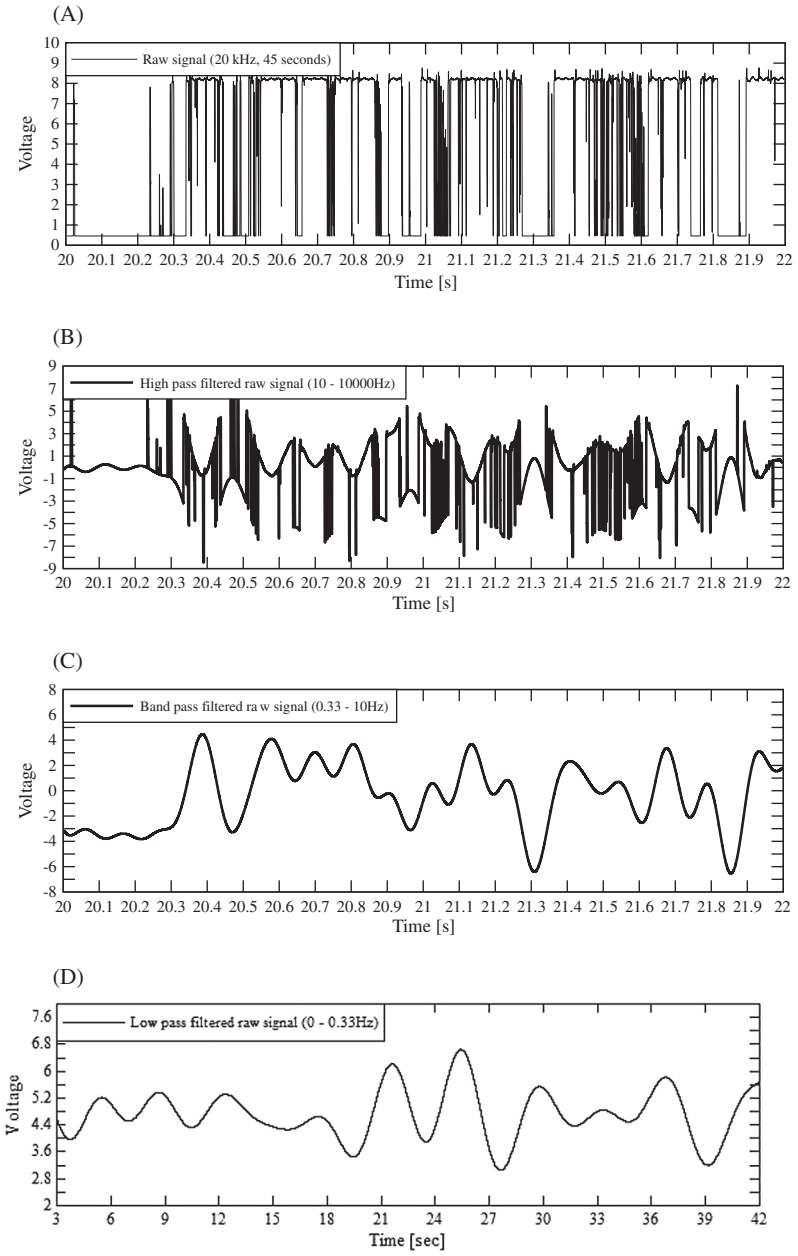

Fig. 3. Raw and filtered signals for $d_c/h = 3.0$, $q_w = 0.182$ m^2/s, Re = 7.2×10^5, (A) raw signal, (B) high pass filtered raw signal (10–10,000 Hz), (C) band pass filtered raw signal (0.33–10 Hz), (D) low pass filtered raw signal (0–0.33 Hz).

The low pass, band pass and high pass filtering of the raw signals were calculated following Press et al. (2007). Fig. 3 illustrates a typical raw probe signal (Fig. 3A) and the resulting components after filtering (Figs. 3B–D). Note the different time axis range for the low pass filtered signal in Fig. 3D. The data set was based upon a complete time series of 39 s at 20 kHz, i.e. 780,000 data points. A 13 s sub-sample was used, thus allowing a sufficiently large data sub-set and proper smoothing of the results.

2.2.2. Decomposition of the air–water properties

The instantaneous void fraction c may be expressed in terms of the decomposed filtered components:

$$c = \tilde{c} + c' + c'' \tag{6}$$

where $\tilde{c}$ is a mean or low pass filtered component, c' represents the slow fluctuating or band pass filtered contribution and c'' is the fast fluctuating or high pass filtered component which is expected to be associated with the 'true' turbulent motion of the flow. The time averaged void fraction C is:

$$C = \frac{1}{n} \times \sum_{1}^{n} (\tilde{c} + c' + c'') = \tilde{C} + C' + C'' \tag{7}$$

where n is the number of data samples. When the lower cut-off frequency (0.33 Hz herein) is significantly smaller than the characteristic frequencies of the air–water flow fluctuations, it yields:

$$C \approx \frac{1}{n} \times \sum_{1}^{n} \tilde{c} = \tilde{C} \tag{8}$$

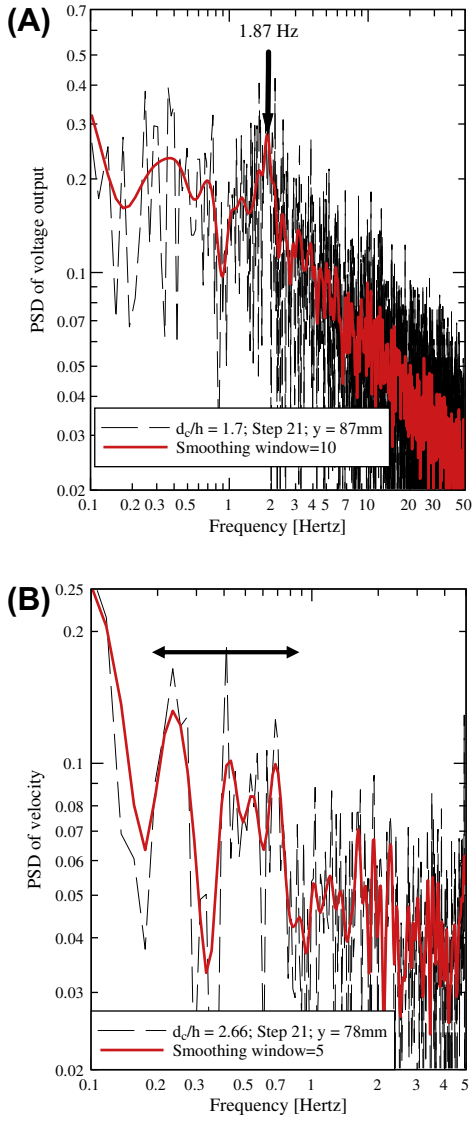

Fig. 4. Spectral analysis of characteristic fluctuations of raw phase-detection probe signals and interfacial velocities of a double-tip conductivity probe, (A) FFT of fluctuations of raw signal of the leading tip probe: $C = 0.812$, $F = 21.0$ Hz, $V = 1.55$ m/s, (B) FFT of fluctuations of the interfacial velocity signal (0.1 s intervals): $C = 0.365$, $F = 69.9$ Hz, $V = 2.43$ m/s.

$$C' = \frac{1}{n} \times \sum_{1}^{n} c' \approx 0 \tag{9}$$

$$C'' = \frac{1}{n} \times \sum_{1}^{n} c'' \approx 0 \tag{10}$$

Using normalised auto- and cross-correlation functions and assuming that $\tilde{c} \approx C$, the decomposed auto- and cross-correlation functions may be linearly decomposed:

$$R_{xx}(\tau) = \alpha \times R_{x'x'}(\tau) + \beta \times R_{x''x''}(\tau) + \chi \times (R_{x'x''}(\tau) + R_{x''x'}(\tau)) \tag{11}$$

$$R_{xy}(\tau) = A \times R_{x'y'}(\tau) + B \times R_{x''y''}(\tau) + D \times R_{x'y''}(\tau) + E \times R_{x''y'}(\tau) \tag{12}$$

where R_{xx} and R_{xy} are the auto- and cross-correlation functions for the raw signal and the decomposed signals respectively, and the factors α, β, χ, A, B, D and E were coefficients of proportionality. In Eqs. (11) and (12), the subscripts x' and y' indicate the band pass filtered signal components of the leading and trailing probe sensors,

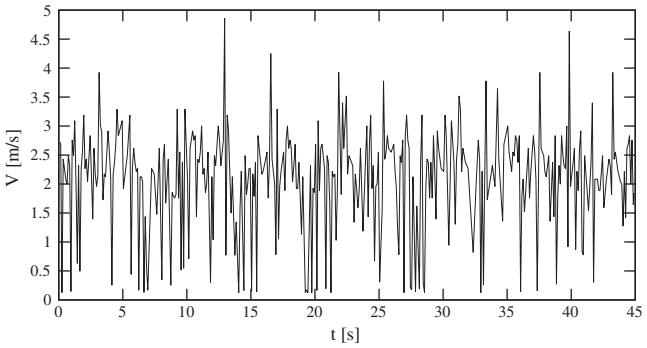

Fig. 5. Interfacial velocity signal of a double-tip conductivity probe calculated for a series of non-overlapping 0.1 s intervals – Flow conditions: $d_c/h = 2.66$, step 21, $y = 78$ mm, $C = 0.365$, $F = 69.9$ Hz, $V = 2.43$ m/s.

and the subscripts x'' and y'' the high pass filtered components of the two sensors. When the characteristic frequencies of the band-pass filtered signal are one or more order(s) of magnitude smaller than the characteristic frequencies of the high-pass filtered signals, the 'cross' terms $R_{x'y''}$ and $R_{x''y'}$ are significantly smaller than the terms $R_{x'y'}$ and $R_{x''y''}$. (Similarly, when the characteristic frequencies of the band-pass filtered signal are one or more order(s) of magnitude larger than the characteristic frequencies of the low-pass filtered signals, the terms $R_{x\bar{y}'}$ and $R_{x'\bar{y}}$ are negligible.) That is, $R_{x'x''} \approx R_{x''x'} \approx R_{x'y''} \approx R_{x''y'} \approx 0$ in first approximation.

The auto-correlation functions may be simplified to:

$$R_{xx}(\tau) \approx \alpha \times R_{x'x'}(\tau) + \beta \times R_{x''x''}(\tau) = R'_{xx}(\tau) + R''_{xx}(\tau) = R^{(1)}_{xx}(\tau) \tag{13}$$

where R'_{xx} and R''_{xx} are the auto-correlation functions of band pass and high pass filtered signals, and $R^{(1)}_{xx}$ is their sum. Similarly Equation (12) becomes:

$$R_{xy}(\tau) \approx A \times R_{x'y'}(\tau) + B \times R_{x''y''}(\tau) = R'_{xy}(\tau) + R''_{xy}(\tau) = R^{(1)}_{xy}(\tau) \tag{14}$$

where R'_{xy} and R''_{xy} are proportional to the cross-correlation functions of band pass and high pass filtered signals, and $R^{(1)}_{xy}$ is the sum of the band and high pass filtered correlation functions: $R^{(1)}_{xy} = R'_{xy} + R''_{xy}$ (Fig. 6). Fig. 6 shows a typical example of the cross-correlation function decomposition.

Since the cross-correlation function can be decomposed linearly, the time-averaged interfacial velocity corresponding to the band pass and high pass filtered signal equals:

$$V' = \frac{\Delta x}{T'} \tag{15}$$

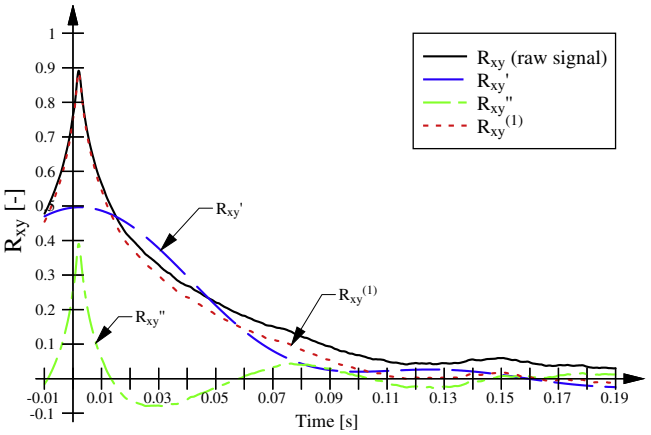

Fig. 6. Cross-correlation functions for the raw signal and the filtered signal components on the pooled stepped spillway: $d_c/h = 3.0$, $q_w = 0.182$ m^2/s, Re = 7.2×10^5; Step edge 20, $y = 102$ mm, $C = 0.715$, $F = 55.9$ Hz.

$$V'' = \frac{\Delta x}{T''} \approx V \tag{16}$$

where T' and T'' are the time lags for which $R_{x'y'}$ and $R_{x''y''}$ were maximum respectively. A further time-averaged interfacial velocity may be calculated:

$$V^{(1)} = \frac{\Delta x}{T^{(1)}} \tag{17}$$

where $T^{(1)}$ is the time for which the sum of the band and high pass filtered correlation functions ($R^{(1)}_{xy} = R'_{xy} + R''_{xy}$, Eq. (14)) was maximum: i.e., $R^{(1)}_{xy}(T^{(1)}) = (R_{xy})^{(1)}_{max}$.

The decomposition of the auto- and cross-correlation functions of the filtered signals is a linear process (Eqs. (13), (14)), and the definition of the auto- and cross-correlation integral time scale becomes:

$$T_{xx} \approx \alpha \times T_{x'x'} + \beta \times T_{x''x''} = T'_{xx} + T''_{xx} \approx T^{(1)}_{xx} \tag{18}$$

$$T_{xy} \approx A \times T_{x'y'} + B \times T_{x''y''} = T'_{xy} + T''_{xy} \approx T^{(1)}_{xy} \tag{19}$$

where T'_{xx} and T'_{xy} are the auto- and cross-correlation time scales for the band pass filtered signal, T''_{xx} and T''_{xy} for the high pass filtered signal, and $T^{(1)}_{xx}$ and $T^{(1)}_{xy}$ for the sum of the band pass and high pass filtered correlation scales. The correlation time scales of the raw function are almost identical to the time scales $T^{(1)}_{xx}$ (and $T^{(1)}_{xy}$) and $T'_{xx} + T''_{xx}$ (and $T'_{xy} + T''_{xy}$) (Felder and Chanson, 2012). That is:

$$T_{xx} \approx T^{(1)}_{xx} \approx T'_{xx} + T''_{xx} \tag{20}$$

$$T_{xy} \approx T^{(1)}_{xy} \approx T'_{xy} + T''_{xy} \tag{21}$$

The turbulence intensity is linked to the broadening of the cross-correlation function relative to the auto-correlation function. Herein the turbulence intensities for the band pass filtered, the high pass filtered signal and for the sum of the cross-correlation functions of band and high pass filtered signals (Eq. (14)) are calculated as:

$$Tu' = 0.851 \times \frac{\sqrt{\tau'^2_{0.5} - T'^2_{0.5}}}{T'} \tag{22}$$

$$Tu'' = 0.851 \times \frac{\sqrt{\tau''^2_{0.5} - T''^2_{0.5}}}{T''} \tag{23}$$

$$Tu^{(1)} = 0.851 \times \frac{\sqrt{\tau^{(1)2}_{0.5} - T^{(1)2}_{0.5}}}{T^{(1)}} \tag{24}$$

Note that Eq. (4) is highly non-linear, and it is not possible to justify a 'classical' turbulent decomposition.

2.2.3. Discussion

The auto- and cross-correlations of the probe signal components are valid representation of the original signal since a linear decomposition is applied (Eqs. (13), (14)). The calculations of auto- and cross-correlation time scales and of interfacial velocities are theoretically justifiable. Yet it is not possible to prove the theoretical validity of the turbulence intensity decomposition (i.e. $Tu = Tu' + Tu''$). However the present results showed that the decomposition of the turbulence levels of the raw data was possible and the results yielded:

$$Tu \approx Tu^{(1)} \tag{25}$$

for all discharges, at each longitudinal cross-section and all elevations (see below). Eqs (22) and (23) further yielded physically meaningful results. The present triple de-composition technique based upon the raw probe signals differs hence from the traditional triple decomposition of velocity signals.

A similar approach in terms of correlation analyses of filtered signals is commonly performed in acoustics where it is called interaural correlation (Trahiotis et al., 2005; Boemer et al., 2011) and in speech recognition (Stern et al., 2007). In fluid mechanics, the use of correlation techniques applied to filtered signals in turbulent flows is mentioned by Favre (1965), Comte-Bellot and Corrsin (1971) and Frisch (1995). Some different triple decomposition approach was also introduced by Telionis (1981) in unsteady viscous flows.

3. Experimental observations

3.1. Presentation

New experiments were conducted on a large size stepped spillway model at the Institute of Hydraulic Engineering and Water Resources Management (IWW), RWTH Aachen University (Germany). The stepped spillway model was previously used by Thorwarth (2008). The test section was a 12 m long, 0.5 m wide channel. At the upstream end, the flow was controlled by a broad crested weir providing a discharge per unit width $0.004 \leqslant q_w \leqslant 0.234$ m^2/s. The test section was equipped with 21 identical PVC steps, with height $h = 0.05$ m and length $l = 0.318$ m, yielding a channel slope $\theta = 8.9°$ (Fig. 7). Two stepped configurations were investigated: (1) flat steps and (2) pooled steps with a pool weir height $w = 0.05$ m (Fig. 7A). The measurements were conducted on the channel centreline at step edges and pool weir edges in the air–water flows downstream of the inception point of free-surface aeration for a range of flow conditions (Table 1).

The air–water measurements were conducted with a double-tip conductivity probe, used previously by Thorwarth (2008) and Bung (2011). The probe sensors had a size of Ø = 0.13 mm and were separated in the flow direction $\Delta x = 5.1$ mm and transverse direction $\Delta z = 1$ mm (Fig. 2). The probe was mounted on a trolley with an electronic control system (isel®) enabling an automatic translation in vertical direction with an accuracy of 0.2 mm. The probe sensors were sampled at 20 kHz per sensor for 45 s. More details about the experimental facility and instrumentation can be found in Felder (2013).

3.2. Basic flow patterns

Some detailed visual flow observations and documentation were conducted for a range of discharges $0.004 \leqslant q_w \leqslant 0.234$ m^2/s, while Table 1 summarises the experimental flow conditions for the detailed air–water flow measurements. Some video movies are available as digital supplementary data (Appendix B).

The air–water flow patterns on the flat stepped spillway showed some typical characteristics, similar to previous studies on stepped spillways (Chanson and Toombes, 2002). For the smaller flow rates ($d_c/h < 0.95$), a nappe flow regime was observed with a succession of free-falling jets (Toombes, 2002). With increasing flow rate ($0.95 < d_c/h < 1.69$), the flow appeared chaotic with some strong splashing in the transition flow regime. For larger flow rates $d_c/h > 1.69$, a skimming flow regime took place with stable cavity recirculation movements. The free-surface was parallel to the pseudo-bottom formed by the step edges in both aerated and non-aerated flow regions (Fig. 7A).

On the pooled stepped spillway, a nappe flow regime was observed with water discharging as a free-falling jet impacting into the underlying step pool for $d_c/h < 1.08$. Some air was entrained in the water filled pool by the plunging jet and the air bubbles were detrained at the free-surface before the next overfall. With

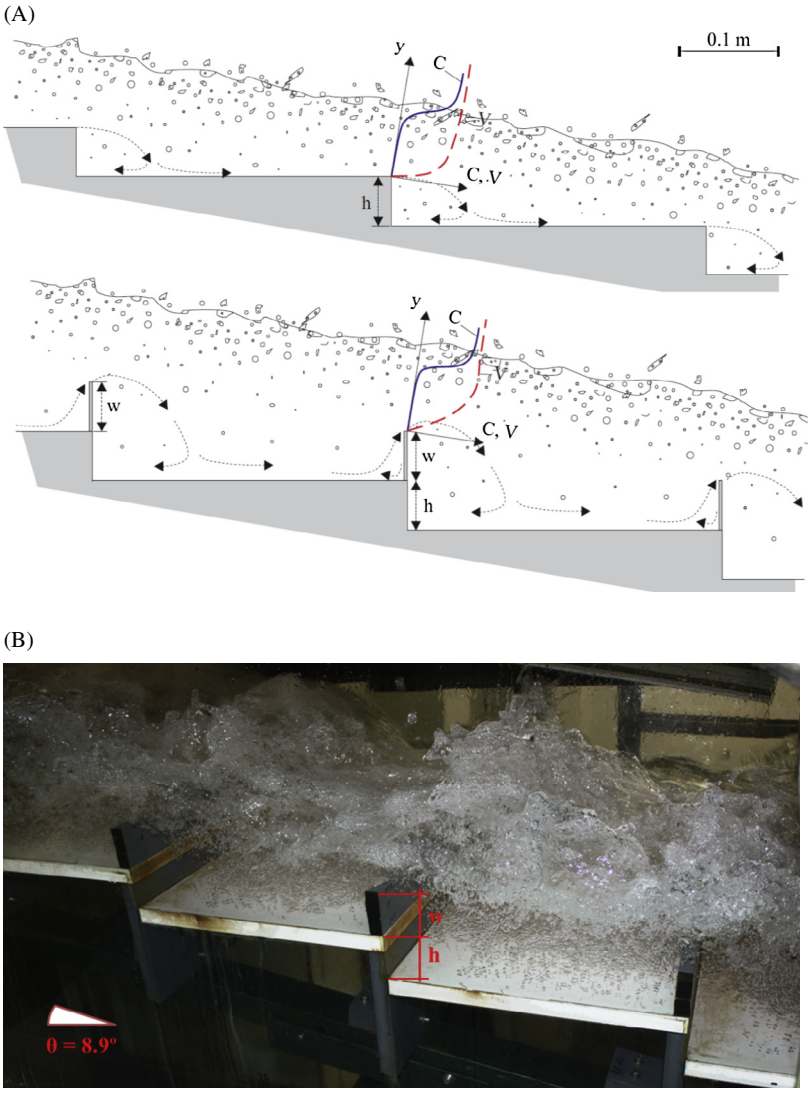

Fig. 7. Air–water flow down the stepped chute (flow from left to right) (A) skimming flow patterns on the flat and pooled step configurations and (B) instationary air–water flows on the pooled stepped spillway: $\theta = 8.9°$, $h = 0.05$ m, $w = 0.05$ m, $d_c/h = 1.71$, $q_w = 0.0784$ m^2/s, Re = 3.1×10^5.

Table 1
Experimental flow conditions for the air–water flow experiments with a double-tip conductivity probe (Ø = 0.13 mm) on the flat and pooled stepped spillways ($\theta = 8.9°$, $h = 0.05$ m, $W = 0.5$ m).

Configuration	w [m]	q_w [m^2/s]	d_c/h [–]	Re [–]
Flat steps	N/A	0.036–0.234	1.0–3.55	1.4×10^5–9.3×10^5
Pooled steps	0.05	0.054–0.234	1.35–3.55	2.2×10^5–9.3×10^5

Note: d_c: critical flow depth; h: vertical step height; Re: Reynolds number defined in terms of the hydraulic diameter; w: pool wall height.

increasing discharge, the flow became unstable in the transition flow regime ($1.08 \leqslant d_c/h \leqslant 1.76$). Some self-induced jump waves were observed for $1.08 \leqslant d_c/h \leqslant 1.76$. Fig. 8A shows some typical instabilities highlighting the unstable jump wave processes including some surface wave propagation and sudden cavity ejections. The frequencies of jump waves were about 0.25–0.4 Hz. Every second jump wave was caused by some pulsating flows in the first step cavity and the other waves were initiated by further instationarities in the first few stepped pools. Video 1 (Movie1_dc_h_1.2.avi) illustrates the pulsating flow in the first step cavity. Video 2 (Movie2_dc_h_1.64.avi) shows the downstream propagation of the surface waves for a larger flow rate (Table 3). Some irregular ejection and recirculation processes within each pooled cavity appeared more often with frequencies of 0.5–2 Hz.

For larger discharges $d_c/h > 1.76$, the jump wave pattern was not present and the flow appeared similar to a skimming flow regime. Downstream of the inception point of free-surface aeration, air was continuously entrained and some recirculation motions in the step cavities were visible and the surface of the air–water flows was overall parallel to the pseudo-bottom (Fig. 7A). However, some instabilities were also seen. Fig. 8B and Video 3 (Movie3_dc_h_2.67.avi) shows examples of instabilities for a typical skimming flow discharge including unstable cavity recirculations, sudden cavity ejections and surface waves. These instabilities appeared to decrease with increasing discharges, but they were still present for the maximum flow rate in the present study ($d_c/h = 3.55$). Through visual observations and video documentation, the unstable processes had characteristic frequencies in the range of 0.5–2 Hz.

3.3. Air–water flow properties

The air–water flow measurements were conducted for all configurations with the same instrumentation and signal processing

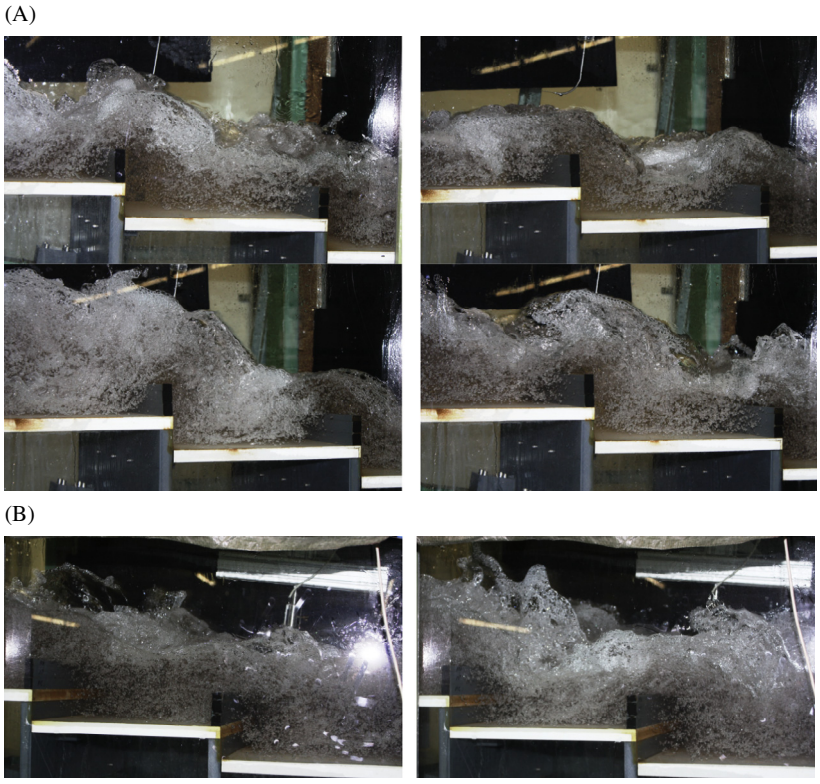

Fig. 8. Flow instabilities on the pooled stepped spillways (A) jump waves in the transition flow regime on the pooled stepped spillway: $d_c/h = 1.35$, $q_w = 0.055$ m^2/s, Re = 2.2×10^5 (photos from left to right and tip to bottom) and (B) instationarities in skimming flow regime on the pooled stepped spillway: $d_c/h = 2.3$, $q_w = 0.122$ m^2/s, Re = 4.9×10^5.

Table 2
Summary of investigated air–water flow parameters in the signal decomposition of free-surface flows.

Parameter	Signal components			
	Raw data	Band pass filtered signal data (0.33–10 Hz)	High pass filtered signal data (10–10,000) Hz	Data calculated based upon weighted sum of correlation functions of band and high pass filtered signal components
Auto-correlation function [–]	R_{xx}	$R'_{xx} = \alpha \times R'_x x'$	$R''_{xx} = \beta \times R_{x''x''}$	$R^{(1)}_{xx} = \alpha \times R_{x'x'} + \beta \times R_{x''x}$
Cross-correlation function [–]	R_{xy}	$R'_{xy} = A \times R'_x y'$	$R''_{xy} = B \times R_{x''y''}$	$R^{(1)}_{xx} = A \times R_{x'y'} + B \times R_{x''y''}$
Cross-correlation time scale [s]	T_{xy}	T'_{xy}	T''_{xy}	$T^{(1)}_{xy}$
Auto-correlation time scale [s]	T_{xx}	T'_{xx}	T''_{xx}	$T^{(1)}_{xx}$
Interfacial velocity [m/s]	V	V'	V''	$V^{(1)}$
Turbulence intensity	Tu	Tu'	Tu''	$Tu^{(1)}$

Table 3
Video movies of self-sustained flow instabilities on the pooled stepped spillway.

Video number	Video name	d_c/h [–]
Video 1	Movie1_dc_h_1.2.avi	1.20
Video 2	Movie2_dc_h_1.64.avi	1.64
Video 3	Movie3_dc_h_2.67.avi	2.67

technique. For the flat stepped spillway, the pseudo-bottom ($y = 0$) was defined by the step edges with y measured perpendicular to the pseudo-bottom. For the pooled stepped spillway, the datum ($y = 0$) was the upper edge of the pool weir. A comparison between flat and pooled stepped spillway flows was performed for a wide range of discharges (Table 1). In this section, the air–water flow properties derived from the raw probe signal are presented.

The void fraction distributions highlighted the strong aeration of the flow. The data showed some typical S-shapes for both flat and pooled stepped spillways in skimming flows (Fig. 9). The results were qualitatively comparable between the two stepped configurations. Some typical void fraction distributions are illustrated in Fig. 9 for several consecutive step edges downstream of the inception point. Fig. 9 shows a self-similar presentation with C as a function of the dimensionless distance above the pseudo-bottom y/Y_{90} with C the void fraction and Y_{90} the characteristic depth where the air concentration is 90%. The void fraction distributions compared well with an analytical solution of the advective diffusion equation for air bubbles in turbulent free-surface flows (Chanson and Toombes, 2002):

$$C = 1 - \tanh^2\left(K' - \frac{y/Y_{90}}{2 \times D_o} + \frac{(y/Y_{90} - 1/3)^3}{3 \times D_o}\right) \quad (26)$$

where K' is an integration constant and D_o is a function of the depth-averaged void fraction C_{mean} only.

The data for both stepped configurations showed some self-similar distributions of dimensionless interfacial velocity V/V_{90} as a function of y/Y_{90}, where V_{90} is the velocity at $C = 90\%$ (Fig. 9).

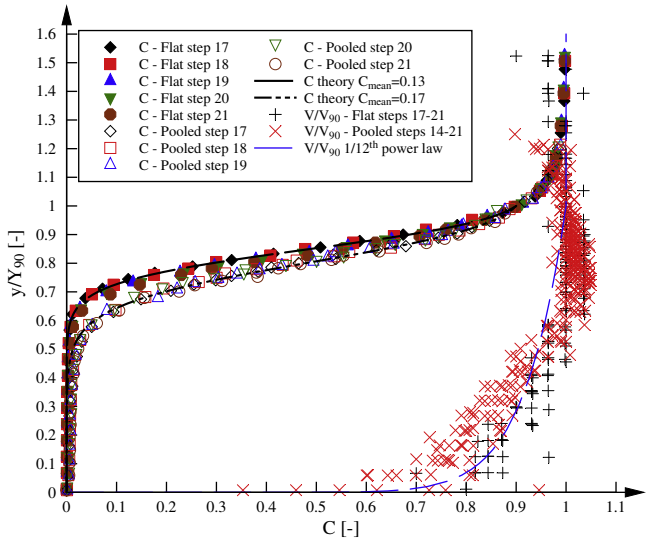

Fig. 9. Dimensionless distributions of void fraction and interfacial velocity on the flat and pooled stepped spillways, Comparison with self-similar equations (Eqs. (26–28)): $d_c/h = 3.55$, $q_w = 0.234$ m^2/s, Re = 9.3×10^5.

Fig. 9 presents some typical velocity data. Despite some scatter, the flat stepped chute velocity data were correlated with a power law:

$$\frac{V}{V_{90}} = \left(\frac{y}{Y_{90}}\right)^{1/N} \quad y/Y_{90} \leq 1 \tag{27}$$

The power law exponent was typically $N = 10$–12 for skimming flows (e.g. Chanson and Toombes, 2002; Chanson and Carosi, 2007; Felder and Chanson, 2011), although the exact value may vary from one step edge to the next one for a given flow rate. In the upper spray region (i.e. $y/Y_{90} > 1$), a uniform velocity profile was observed as shown by earlier studies:

$$\frac{V}{V_{90}} = 1 \quad y/Y_{90} > 1 \tag{28}$$

Both Eqs (27) and (28) are compared with experimental data in Fig. 9.

On the pooled stepped chute, the velocity data differed from the power law. It is likely that the differences were attributed to the velocity redistribution between the cavity and the pool edge, as sketched in Fig. 7A.

The vertical distributions of bubble count rate, and auto- and cross-correlation time scales showed characteristic shapes on both pooled and flat stepped spillways, with maximum values in the intermediate flow region ($0.3 < C < 0.7$). In the bubbly flow region ($C < 0.3$) and the spray region ($C > 0.7$), the bubble frequency and the time scales tended towards very small values for large void/liquid fractions. The comparative analyses of bubble count rate and auto- and cross-correlation integral time scales showed some marked differences in magnitude between flat and pooled stepped spillways. Fig. 10 shows some typical dimensionless bubble count rate distributions $F \times d_c/V_c$ where F is the bubble count rate, d_c is the critical flow depth and V_c is the critical flow velocity. (In open channel hydraulics, d_c and V_c are respectively defined as $d_c = (q_w^2/g)^{1/3}$ and $V_c = (q_w \times g)^{1/3}$ (Henderson, 1966).) Fig. 10A shows a comparison of vertical distributions of bubble count rate for both configurations as functions of y/Y_{90}. The most distinctive difference was the larger dimensionless bubble frequencies on the flat stepped spillway compared to those recorded in the pooled stepped spillway across the entire air–water column. Fig. 10B presents the dimensionless relationship between time-averaged void fraction and bubble count rate for spooled stepped chute. The data

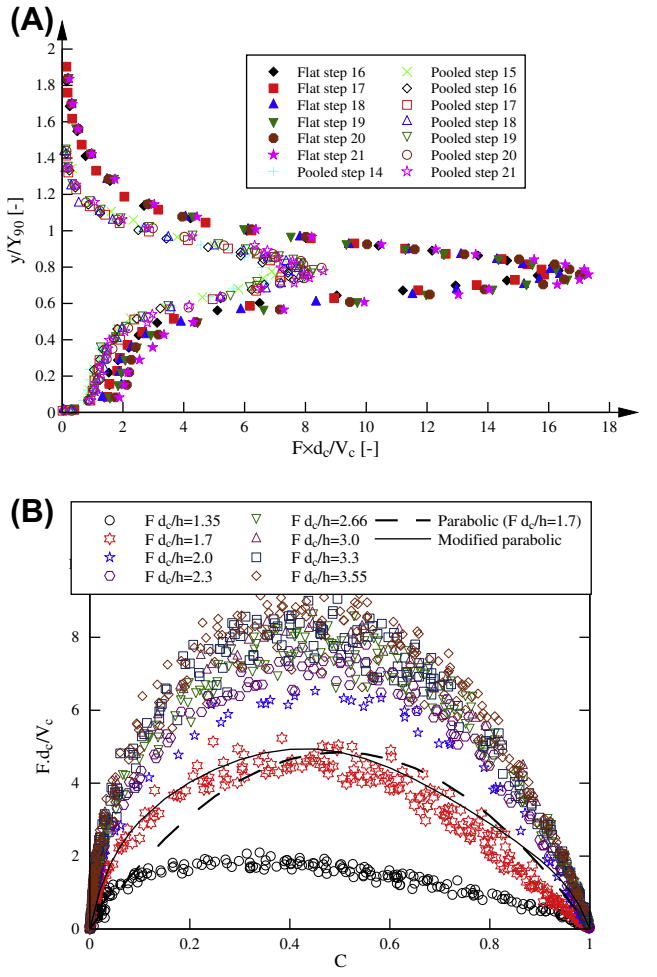

Fig. 10. Dimensionless distributions of bubble count rate (A) vertical distributions of bubble count rate on the flat and pooled stepped spillways: $d_c/h = 2.66$, $q_w = 0.152$ m^2/s, Re = 6.0×10^5 and (B) dimensionless relationship between bubble count rate and time-averaged void fraction on pooled stepped chute – Comparison with parabolic law and theoretical model of Toombes and Chanson (2008) for $d_c/h = 1.7$, $q_w = 0.076$ m^2/s, Re = 3.0×10^5.

showed a pseudo-parabolic relationship which compared well with the theoretical model of Toombes and Chanson (2008).

The auto- and cross-correlation integral time scale data showed also some differences (Fig. 11). In Fig. 11A, the dimensionless auto-correlation time scales $T_{xx} \times \text{sqrt}(g/Y_{90})$ are presented as a function of y/Y_{90}. The dimensionless time scales on the pooled stepped spillway were about three to four times larger than the time scales on the flat stepped spillway. A similar finding is seen in Fig. 11B in terms of the cross-correlation time scales $T_{xy} \times \text{sqrt}(g/Y_{90})$. The dimensionless cross-correlation integral time-scales were about five to seven times larger on the pooled stepped spillway.

Some distinctive differences between pooled and flat spillway configurations were observed in terms of the turbulence intensity Tu in the air–water flow region (Fig. 12). Fig. 12A illustrates these differences in a self-similar presentation as a function of y/Y_{90}. On the pooled stepped spillway, the turbulence levels were significantly larger. The maximum turbulence levels reached up to 600% in the intermediate flow region on the pooled stepped spillway, compared to 150–200% on the flat stepped spillway. In the lower bubbly flow region and the upper spray region, the turbulence levels tended towards about 20–40% for both configurations as shown by Chanson and Toombes (2002). The relationship between turbulence levels and dimensionless bubble count rate is

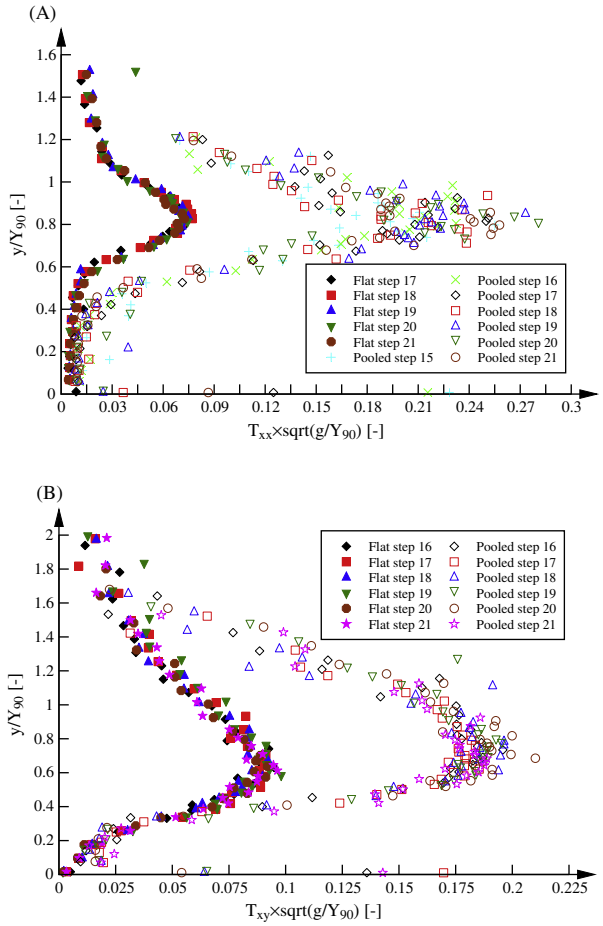

Fig. 11. Dimensionless distributions of auto- and cross-correlation time scales on the flat and pooled stepped spillways (A) auto-correlation time scales: $d_c/h = 3.55$, $q_w = 0.234$ m^2/s, Re = 9.3×10^5 (B) cross-correlation time scales: $d_c/h = 1.71$, $q_w = 0.078$ m^2/s, Re = 3.1×10^5.

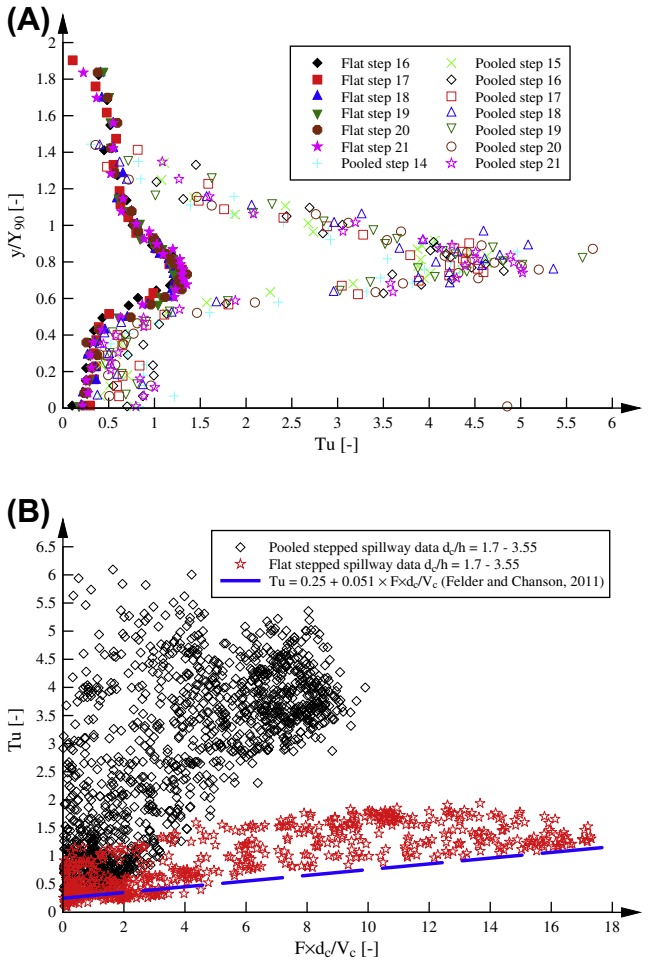

Fig. 12. Turbulence intensity on the flat and pooled stepped spillways (A) turbulence intensity distribution: $d_c/h = 2.66$, $q_w = 0.152$ m^2/s, Re = 6.0×10^5 and (B) relationship between turbulence intensity and bubble count rate for all skimming flow data – Comparison with best-fit equation (Felder and Chanson, 2011).

shown in Fig. 12B for both configurations as well as an empirical correlation of a flat stepped spillway (Felder and Chanson, 2011). The present data on the flat stepped spillway were qualitatively in agreement with earlier findings, but the pooled stepped spillway data showed a very different pattern (Fig. 12B). The turbulence levels on the pooled stepped spillway were drastically larger and it is believed that this was linked to the presence of slow hydrodynamic fluctuations and instabilities.

4. Triple decomposition technique application

For all experimental data on the pooled stepped spillway in presence of instability, the triple decomposition was applied to the raw probe signals. The cut-off frequencies of 0.33 and 10 Hz were used. The results are presented below in terms of the calculations based upon (a) the raw signal, (b) the band pass filtered signal, i.e. the slow fluctuating signal component, (c) the high pass filtered signal, i.e. the fast fluctuating signal component, and (d) the calculations based upon the sum of slow and fast fluctuating signal correlations. The notation reflects the decomposition method: for example, with V the time-averaged interfacial velocity calculated from the raw signal, V' the slow fluctuating component of the velocity calculated from the band-pass filtered signal, V'' the fast fluctuating velocity component computer from the high-pass filtered signal, and $V^{(1)}$ the velocity calculated from the weighted sum of correlation functions of band and high pass filtered signal components (Eqs. (15)–(17)). Table 2 summarises the parameters investigated in this section.

The auto- and cross-correlation functions were calculated for 4000 time steps (i.e. time lag $0 < \tau < 0.2$ s) which appeared an optimum in terms of data quality and calculation time. A typical cross-correlation function is shown in Fig. 6. Fig. 6 includes the cross-correlation functions of the raw data (R_{xy}), of the band pass filtered signal (R'_{xy}), of the high pass filtered signal (R''_{xy}) and of the summation of the correlation functions of band and high pass filtered signals ($R^{(1)}_{xy}$).

For all investigated flow conditions (Table 1) and vertical elevations within the water column, the shapes of the raw signal cross-correlation function were in agreement with results from previous stepped spillway studies (Carosi and Chanson, 2006), but the time lag for the first crossing was relatively longer. The shape of the cross-correlation functions for the band pass filtered signal showed a different shape for small time lags, with a plateau of largest cross-correlation values (Fig. 6, thick blue dashed curve). The shape for the high pass filtered component was much steeper for small time lags: e.g., $\tau < 0.01$ s in Fig. 6. The summation of cross-correlation functions of band and high pass filtered components was close to the cross-correlation function of the raw signal, although the curve was consistently slightly lower (Fig. 6, thick red dotted curve). Similar results were found in terms of the auto-correlation functions not shown herein.

4.1. Auto- and cross-correlation time scales

The cross-correlation integral time scales were calculated for the raw signal and the decomposed signal components. A typical result is shown in Fig. 13. The distributions of integral time scales showed the largest values were seen in the intermediate flow region ($0.3 < C < 0.7$), with T_{xy} tending towards zero in the bubbly flow region and smaller values of T_{xy} in the spray region (e.g. Fig. 13, raw signal data (black squares)). For all flow conditions (Table 1), at all longitudinal locations and vertical elevations, the distributions of integral time scales were qualitatively in good agreement and similar to previous studies on stepped chutes (Chanson and Carosi, 2007; Felder and Chanson, 2009).

The smallest integral time scale data were obtained for the high pass filtered signal component, T''_{xy} (e.g. Fig. 13, green diamonds). For $0.3 < C < 0.7$, T''_{xy} was about an order of magnitude smaller than the raw signal data. The integral time scales calculated based upon the band-pass filtered signal, T'_{xy}, and those calculated from the sum of the band- and high-pass filtered signals, $T^{(1)}_{xy}$, were comparable to the raw data (e.g. Fig. 13). The auto-correlation integral time scale data showed similar results, with the high pass filtered signal data, T''_{xx}, being about an order of magnitude smaller than the band-pass filtered data and raw data (Fig. 14). The auto-correlation time scales of the raw signal, the band pass filtered signal component, T'_{xx}, and of the sum $T^{(1)}_{xx}$, were close with maximum time scales in the intermediate flow region ($0.3 < C < 0.7$) and smaller values in the lower bubbly and upper spray regions.

Overall the results tended to confirm the linearity of the decomposition process for the auto- and cross-correlation time scales for all investigated flow conditions (Table 1).

4.2. Interfacial velocity

The velocity data calculated based upon the raw signal were similar to previous studies on pooled stepped spillways (Kökpinar, 2004; Thorwarth, 2008). A typical vertical distribution of time-averaged interfacial velocity is presented in Fig. 15 including the raw signal analysis and the decomposed components.

For all investigations, the time-averaged velocity results showed $V = V'' = V^{(1)}$. This 'apparently surprising' outcome was believed to be linked with some basic geometrical considerations. The distance between probe sensors was $\Delta x = 5.1$ mm, and the interfacial velocities ranged between 1 and 5 m/s. For these conditions, the interface travel time ranged from 1 to 5 ms (e.g. 1.5–3 ms

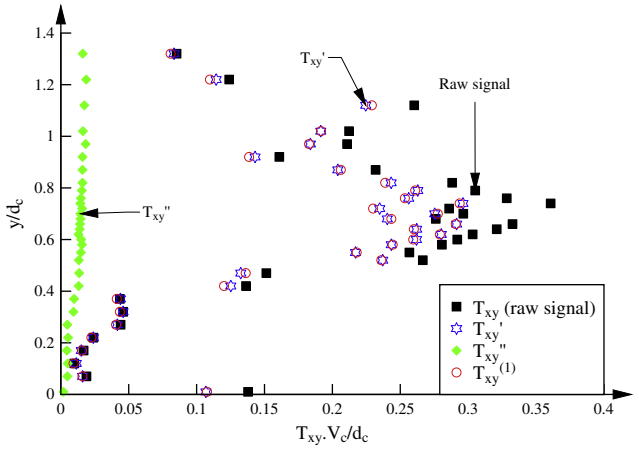

Fig. 13. Cross-correlation time scale distributions for the raw signal and the filtered signal components on the pooled stepped spillway: $d_c/h = 2.0$, $q_w = 0.099$ m^2/s, Re = 3.9×10^5; Step edge 21.

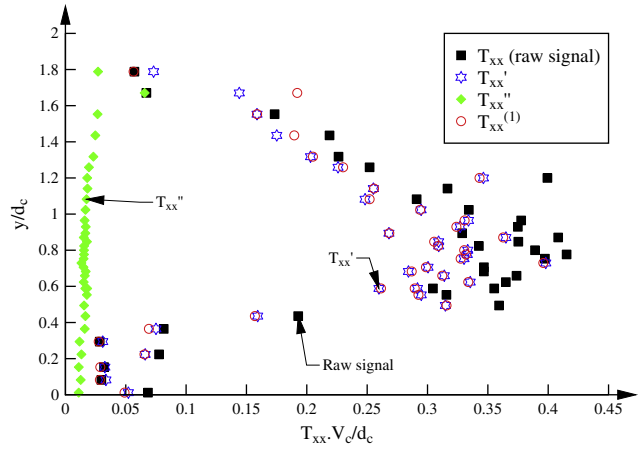

Fig. 14. Auto-correlation time scale distributions for the raw signal and the filtered signal components on the pooled stepped spillway: $d_c/h = 1.7$, $q_w = 0.078$ m^2/s, Re = 3.1×10^5; Step edge 20.

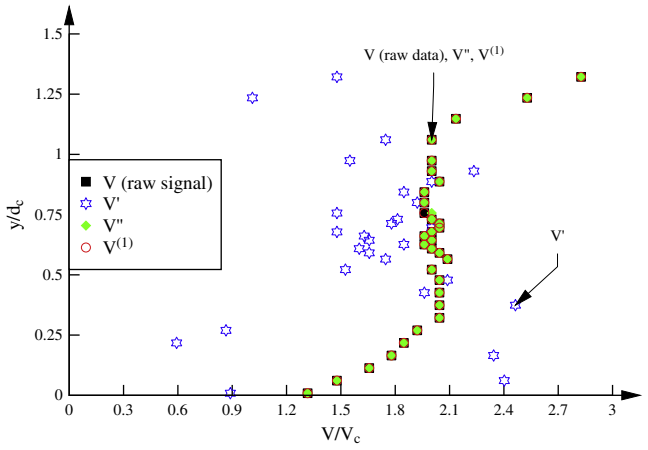

Fig. 15. Interfacial velocity distributions for the raw signal and the filtered signal components on the pooled stepped spillway: $d_c/h = 2.3$, $q_w = 0.122$ m^2/s, Re = 4.9×10^5; Step edge 19.

in Fig. 15), corresponding to characteristic frequencies (200–1000 Hz) within the high-pass filtered frequency range (10–10,000 Hz). In turn the band-pass filtered data could not accurately determine the interfacial velocity because the cross-correlation function calculated based upon the band-pass filtered signal had a very flat peak (see Fig. 6). The very flat peak prevented an accurate estimate of T', hence V'. The finding is illustrated in Fig. 15, in which the slow fluctuating velocity component V' exhibited some scatter in the bubbly and spray regions.

4.3. Turbulence intensity

In the pooled stepped chute, the two-phase flow properties were recorded for over 1600 sampling points for a wide range of flow conditions (Table 1). Fig. 16 presents some typical comparative results at a cross-section for one flow rate. All the turbulence intensity results are reported in Fig. 17, showing a comparison between calculations based upon the raw probe signal and turbulence levels calculated based upon the band and high pass filtered signals on the pooled stepped spillway. Fig. 17 regroups the ratios Tu'/Tu, $Tu^{(1)}/Tu$ and $(Tu' + Tu'')/Tu$ as functions of the time-averaged void fraction C for all the data points. In addition, the dimensionless bubble count rate data are shown for comparison in Fig. 17B.

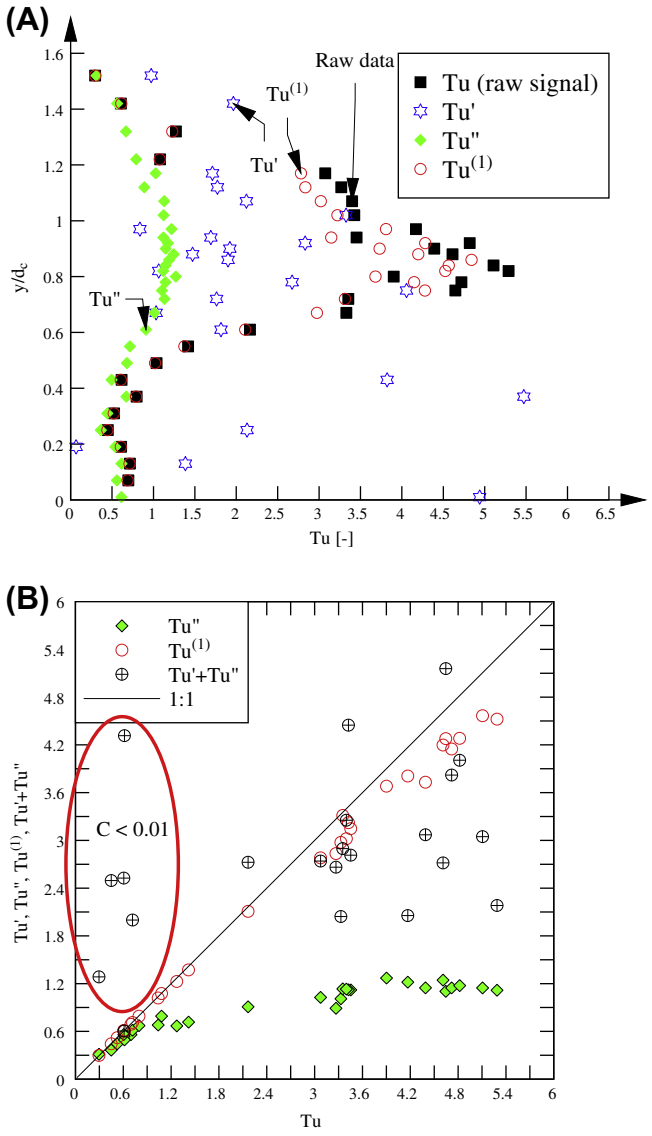

Fig. 16. Turbulence intensity results for the raw signal and the filtered signal components on the pooled stepped spillway: $d_c/h = 2.66$, $q_w = 0.152$ m^2/s, Re = 6.0×10^5; Step edge 19 (A) vertical distributions (B) relationship between the turbulence intensity data for the raw signal and the filtered signal components – Red highlight correspond to sampling points where $C < 0.01$.

The fast fluctuating turbulence intensity data Tu'' had a shape close to that of the raw signal data Tu, with maxima in terms of turbulence intensity in the intermediate flow region (Fig. 16). However the maximum values $(Tu'')_{max}$ were about 120%, compared to $Tu_{max} \sim 600\%$ for the raw signal data. The turbulence intensities calculated based upon the weighted sum of the correlation functions of band pass and high pass filtered signal components were close to the raw signal results: $Tu \approx Tu^{(1)}$ (Fig. 17A). The sum $(Tu' + Tu'')$ of the band pass and the high pass filtered turbulence levels were smaller than the raw signal data at most positions (Fig. 17B). On average the pooled stepped data gave quantitative values of Tu'' of the same order of magnitude as the turbulence levels observed on the flat stepped chute for the flow rate and longitudinal location (see below).

Overall the results showed consistent trends independently of flow rate (hence Reynolds number) and longitudinal location. For $0.05 < C < 0.95$, the results yielded the key findings:

$$\frac{Tu''}{Tu} = 0.28 \qquad \text{Std} = 0.079 \text{ for } 991 \text{ points} \tag{29}$$

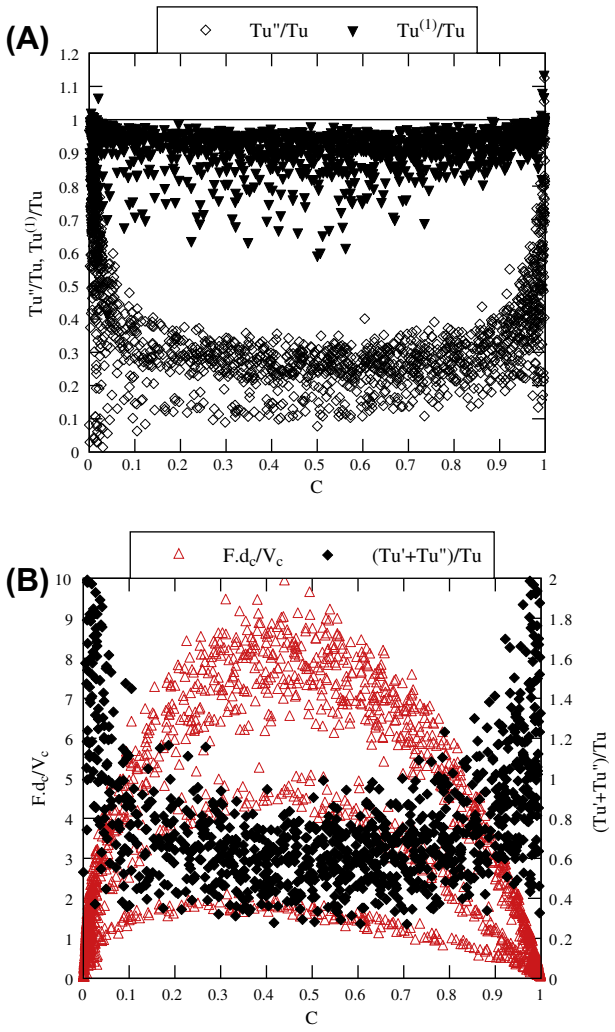

Fig. 17. Comparison of the turbulence intensity calculated based upon the raw probe signal to the turbulence levels calculated based upon the band and high pass filtered signals on the pooled stepped spillway (all data sets: 1667 data points) (A) ratios Tu''/Tu and $Tu^{(1)}/Tu$ as functions of the local void fraction (B) ratio $(Tu' + Tu'')/Tu$ and dimensionless bubble frequency $F \times d_c/V_c$ as functions of the local void fraction.

$$\frac{Tu^{(1)}}{Tu} = 0.93 \qquad \text{Std} = 0.063 \text{ for } 1134 \text{ points} \tag{30}$$

$$\frac{Tu' + Tu''}{Tu} = 0.66 \qquad \text{Std} = 0.249 \text{ for } 849 \text{ points} \tag{31}$$

Note that all the turbulence calculations exhibited significant data scatter for $C < 0.025$–0.05 and $C > 0.95$–0.975 (Fig. 17) because of the small number of air–water interfaces at very low void and liquid fractions.

5. Discussion

The triple decomposition approach was applied herein to instationary air–water flows on a pooled stepped spillway. The decomposition technique enabled the identification of the various flow components into the turbulent kinetic energy. The 'true' turbulence levels were calculated in terms of the fast fluctuating velocity component, while the largest contribution to the turbulent kinetic energy was encompassed within the slow fluctuating component.

For the pooled stepped spillway in presence of flow instabilities, the turbulence levels may be compared with the turbulence intensity measurements observed in flat stepped spillways with a same

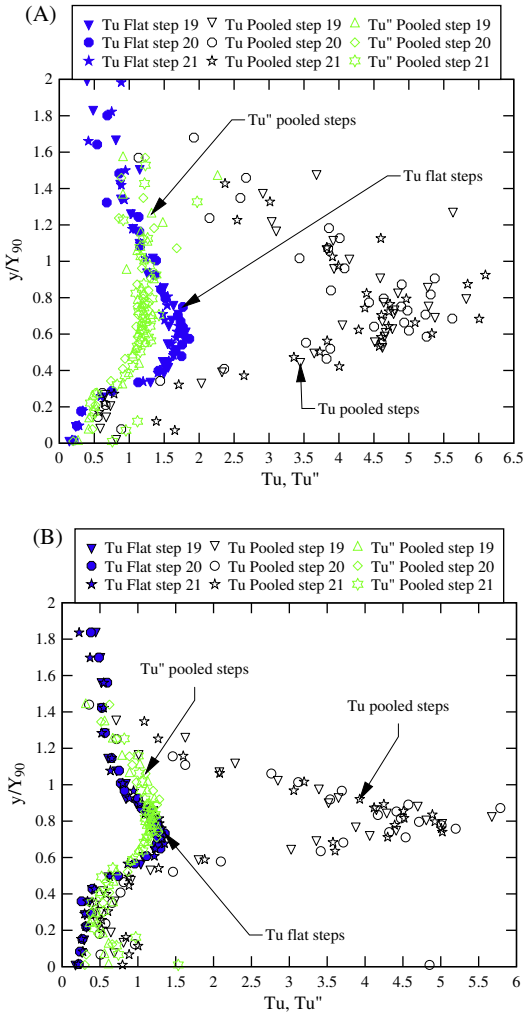

Fig. 18. Comparison between the fast fluctuating component (Tu'') of turbulence intensity on pooled stepped spillway and the turbulence intensity (Tu) on flat stepped spillway (A) $d_c/h = 1.7$, $q_w = 0.0776$ m^2/s, Re = 3.1×10^5; step edges 19–21 (B) $d_c/h = 2.66$, $q_w = 0.152$ m^2/s, Re = 6.0×10^5; step edges 19–21.

slope and for the same flow conditions (Fig. 18). Fig. 18 shows such a comparison. The results suggested that the turbulence levels calculated based upon the high pass filtered signals on pooled steps were of the same magnitude as the turbulence levels observed on flat stepped chute flows (Fig. 18).

Although no theoretical validation was obtained, the experimental results suggested that the decomposition technique yielded some quantitatively meaningful estimates of fast fluctuating turbulent intensity components. Thus the results hinted that a large proportion of the turbulent kinetic energy was encompassed in the slow velocity motion on the pooled stepped spillway in presence of quasi-periodic surges.

6. Conclusion

A new turbulence decomposition technique was introduced herein to quantify the relative contributions of the slow- and fast fluctuations to the flow turbulence in a highly-aerated free-surface flow. The raw signal of the phase-detection probe leading and trailing tips was decomposed linearly using low pass, band pass and high pass filtering of raw probe signals, corresponding to the mean signal component and the slow- and fast-fluctuating components respectively. Some theoretical considerations suggested that the low pass filtered signal component did not contribute to the air–water flow properties, but the time-averaged void fraction.

The results were applied to the analysis of new physical experiments on a relatively large stepped channel with two stepped configurations: that is, flat and pooled steps. No instability was observed on the flat stepped chute, but the pooled stepped chute flow exhibited some self-sustained instabilities, with a range of characteristic frequencies between 0.5 and 2 Hz (digital video Appendix B). For these physical experiments, the cut-off frequencies of 0.33 Hz and 10 Hz were identified based upon both visual observations and frequency analyses. The application of the signal decomposition technique indicated that the turbulence generated by the fast fluctuations was close to that observed in absence in instability and corresponded to less than 30% of the gross turbulence level. Thus the turbulent kinetic energy of the unstable air–water flow motion was mostly encompassed in the slow fluctuating signal component.

Altogether the study demonstrated a successful application of the decomposition technique to gas–liquid flows in industrial applications with high void fractions. To date the method was applied to pooled stepped spillway, and it is believed that there are further potential applications to pseudo-periodic and instationary gas–liquid flows. Examples might encompass the hydraulic jumps and plunging jets, unsteady air–water flows such as surges caused by dam breaks, wave breaking, possibly unsteady cavitation processes.

Acknowledgements

The authors thank Prof. Jorge Matos (IST Lisbon) and Dr. Frédéric Murzyn (ESTACA-Laval) for their valuable inputs, and the reviewers for their helpful comments. They thank Professor Holger Schüttrumpf (IWW, RWTH Aachen University) for providing access to the experimental facility. The first author acknowledges the support through a UQ research scholarship and the (UQ) Graduate School International Travel Award for undertaking the research at IWW. The financial support of the Australian Research Council (Grant DP120100481) is acknowledged.

Appendix A. Turbulence intensity in air–water flows

The turbulence intensity is defined as the ratio of the velocity standard deviation to the time-averaged velocity: $Tu = v'/V$. When the velocity is measured with a dual-tip probe, the standard deviation of the interfacial velocity equals:

$$v'^2 = \frac{1}{n} \times \sum_{i=1}^{n} (v_i - V)^2 = \frac{V^2}{n} \times \sum_{i=1}^{n} \left(\frac{t_i - T}{t_i} \right)^2 \quad \text{(A-1)}$$

where v_i is the instantaneous velocity data equal to $\Delta x/t_i$, V is the time-averaged velocity ($V = \Delta x/T$), n is the number of interfaces, t_i is the interface travel time data and T is the travel time for which the cross-correlation function is maximum. With an infinitely large number n of interfaces, an extension of the mean value theorem for definite integrals may be used as $1/t_i^2$ and $(t_i - T)^2$ are positive and continuous functions over the interval $i = (1, n)$ (Spiegel, 1974). The result implies that there exists at least one characteristic travel time t' satisfying $t_1 \leqslant t' \leqslant t_n$ such that:

$$\left(\frac{v'}{V} \right)^2 = \frac{1}{n} \times \frac{1}{t'^2} \times \sum_{i=1}^{n} (t_i - T)^2 = \frac{\sigma_t^2}{t'^2} \quad \text{(A-2)}$$

where σ_t is the standard deviation of the interface travel time. If the intrinsic noise of the probe signal is un-correlated to the turbulent velocity fluctuations with which the bubbles are convected, the standard deviation of the cross-correlation function σ_{xy} satisfies:

$$\sigma_{xy}^2 = \sigma_{xx}^2 + \sigma_t^2 \quad \text{(A-3)}$$

where σ_{xx} is the standard deviation of the autocorrelation function (Harvey, 1993). The turbulent intensity becomes:

$$\frac{v'}{V} = \frac{\sqrt{\sigma_{xy}^2 - \sigma_{xx}^2}}{t'} \quad \text{(A-4)}$$

Assuming that $t' \sim T$, the turbulence intensity v'/V equals:

$$Tu = \frac{v'}{V} = \frac{\sqrt{\sigma_{xy}^2 - \sigma_{xx}^2}}{T} \quad \text{(A-5)}$$

Kipphan (1977) developed a similar result for two-phase mixtures such as pneumatic conveying, while the above development follows Chanson and Toombes (2002).

Assuming that the successive detections of bubbles by the probe sensors are a true random process, the cross-correlation function is a Gaussian distribution:

$$R_{xy}(\tau) = (R_{xy})_{max} \times \exp\left(-\frac{1}{2} \times \left(\frac{\tau - T}{\sigma_{xy}}\right)^2\right) \quad \text{(A-6)}$$

After simplification the cross-correlation time scale becomes:

$$T_{xy} = (R_{xy})_{max} \times \sqrt{\frac{\pi}{2}} \times \sigma_{xy} \quad \text{(A-7)}$$

Similarly, if the auto-correlation function is a Gaussian distribution, the auto-correlation time scale becomes:

$$T_{xx} = \sqrt{\frac{\pi}{2}} \times \sigma_{xx} \quad \text{(A-8)}$$

Using Eqs. (A-7) and (A8), the turbulent intensity may be expressed as:

$$Tu = \frac{\sqrt{2}}{\sqrt{\pi} \times T} \times \sqrt{\left(\frac{T_{xy}}{(R_{xy})_{max}}\right)^2 - T_{xx}^2} \quad \text{(A-9)}$$

Assuming that the cross-correlation function is a Gaussian distribution and defining $\tau_{0.5}$ the time scale for which: $R_{xy}(T + \tau_{0.5}) = -R_{xy}(T)/2$, the standard deviation of the cross-correlation function equals: $\sigma_{xy} = \tau_{0.5}/1.175$, while the standard deviation of the auto-correlation function equals: $\sigma_{xx} = T_{0.5}/1.175$ where $T_{0.5}$ is the characteristic time for which the normalised auto-correlation function equals 0.5. Eq. (A-9) yields (Chanson and Toombes, 2002):

$$\frac{v'}{V} = 0.851 \times \frac{\sqrt{\tau_{0.5}^2 - T_{0.5}^2}}{T} \quad \text{(A-10)}$$

Appendix B. Supplementary material

Detailed experimental measurements were conducted in a pooled stepped spillway with a slope $\theta = 8.9°$. A series of short movies were further taken during the experiments using a digital video camera to illustrate the self-sustained flow instabilities on the pooled stepped spillway. The digital appendix includes three movie files (Table 3). Video 1 (Movie1_dc_h_1.2.avi) presents the pulsating flow in the first step cavity. Video 2 (Movie2_dc_h_1.64.avi) shows some hydrodynamic instabilities highlighting the unstable jump wave processes including some surface wave propagation and sudden cavity ejections propagating down the stepped chute. Video 3 (Movie3_dc_h_2.67.avi) illustrates some instabilities for a typical skimming flow discharge including unstable cavity recirculations, sudden cavity ejections and surface waves.

Supplementary data associated with this article can be found, in the online version, at http://dx.doi.org/10.1016/j.ijmultiphaseflow.2013.09.006.

References

Armenio, A., La Rocca, M., 1996. On the analysis of sloshing of water in rectangular containers: numerical study and experimental validation. Ocean Eng. 23 (8), 705–739. http://dx.doi.org/10.1016/0029-8018(96)84409-X.

Boemer, J.I., Oode, S., Ando, A., 2011. Effect of frequency bandwidth on interaural cross-correlation in relation to sound image width of reproduced sounds of a violin. Appl. Acoust. 72, 623–631.

Bradley, J.N., Peterka, A.J., 1957. The hydraulic design of stilling basins: stilling basin and wave suppressors for canal structures, outlet works and diversion dams (basin IV). J. Hydraul. Div. ASCE 83 (5), 1404-1–1404-20.

Brown, R., Chanson, H., 2013. Turbulence and suspended sediment measurements in an urban environment during the Brisbane River Flood of January. J. Hydraul. Eng. ASCE 139 (2), 244–252 (DOI: 10.1061/(ASCE)HY.1943-7900.0000666).

Bung, D.B., 2011. Developing flow in skimming flow regime on embankment stepped spillways. J. Hydraul. Res. 49, 639–648.

Cain, P., 1978. Measurements within Self-Aerated Flow on a Large Spillway. Ph.D. Thesis, Ref. 78-18, Dept. of Civil Engrg., Univ. of Canterbury, Christchurch, New Zealand.

Cain, P., Wood, I.R., 1981. Measurements of self-aerated flow on a spillway. J. Hydraul. Div. ASCE 107 (HY 11), 1425–1444.

Carosi, G., Chanson, H., 2006. Air-water time and length scales in skimming flow on a stepped spillway. Application to the Spray Characterisation. Report No. CH59/06, Division of Civil Engineering, The University of Queensland, Brisbane, Australia, July, 142 pages.

Cartellier, A., 1992. Simultaneous void fraction measurement, bubble velocity, and size estimate using a single optical probe in gas-liquid tow-phase flows. Rev. Sci. Instrum. 63 (11), 5442–5453.

Chanson, H., 1996. Prediction of the transition nappe/skimming flow on a stepped channel. J. Hydraul. Res., IAHR 34, 421–429.

Chanson, H., 1997. Air Bubble Entrainment in Free-Surface Turbulent Shear Flows. Academic Press, London, UK, p. 401.

Chanson, H., 2001. The Hydraulics of Stepped Chutes and Spillways. Balkema, Lisse, The Netherlands, p. pp. 418.

Chanson, H., 2002. Air-water flow measurements with intrusive phase-detection probes can we improve their interpretation? J. Hydraul. Eng., ASCE 128 (3), 252–255.

Chanson, H., 2013. Hydraulics of aerated flows: Qui Pro Quo? J. Hydraul. Res., IAHR 51 (3), 223–243. http://dx.doi.org/10.1080/00221686.2013.795917, Invited Vision paper.

Chanson, H., Carosi, G., 2007. Turbulent time and length scale measurements in high-velocity open channel flows. Exp. Fluids 42, 385–401. http://dx.doi.org/10.1007/s00348-006-0246-2.

Chanson, H., Felder, S., 2010. Turbulence Measurements in Air-Water Self-Aerated Flows: Basic Analysis and Results. In: Proc. 7th International Conference on Multiphase Flow ICMF 2010, Tampa FL, USA, May 30–June 4, Paper No. 10.3.4, 11 pages (USB Memory Stick).

Chanson, H., Toombes, L., 2002. Air-water flows down stepped chutes: turbulence and flow structure observations. Intl. J. Multiph. Flow 28, 1737–1761.

Comte-Bellot, G., Corrsin, S., 1971. Simple Eulerian time correlation of full- and narrow-band velocity signals in grid-generated, 'isotropic' turbulence. J. Fluid Mech. 48, 273–337.

Elviro, V., Mateos, C., 1995. Spanish Research into Stepped Spillways. Int. J. Hydropower Dams 2, 61–65.

Favre, A.J., 1965. Review on space-time correlations in turbulent fluids. J. Appl. Mech. 32, 241–257.

Felder, S., 2013. Air-Water Flow Properties on Stepped Spillways for Embankment Dams: Aeration, Energy Dissipation and Turbulence on Uniform, Non-Uniform and Pooled Stepped Chutes. Ph.D. thesis, School of Civil Engineering, The University of Queensland, Australia.

Felder, S., Chanson, H., 2009. Turbulence, dynamic similarity and scale effects in high-velocity free-surface flows above a stepped chute. Exp. Fluids 47, 1–18. http://dx.doi.org/10.1007/s00348-009-0628-3.

Felder, S., Chanson, H., 2011. Air-water flow properties in step cavity down a stepped chute. Intl. J. Multiph. Flow 37, 732–745. http://dx.doi.org/10.1016/j.ijmultiphaseflow.2011.02.009.

Felder, S., Chanson, H., 2012. Air-Water Flow Measurements in Instationary Free-Surface Flows: a Triple Decomposition Technique. Hydraulic Model Report No. CH85/12, School of Civil Engineering, The University of Queensland, Brisbane, Australia, 151 pages.

Fox, J.F., Papaniclaou, A.N., Kjos, L., 2005. Eddy taxonomy methodology around submerged barb obstacle within a fixed rough bed. J. Eng. Mech., ASCE 131, 1082–1101.

Frisch, U., 1995. Turbulence: The Legacy of A.N. Kolmogorov. Cambridge University Press, 312 pages.

Harvey, A.C., 1993. Time Series Models. Harvester Wheatsheaf, London.

Henderson, F.M., 1966. Open Channel Flow. MacMillan Company, New York, USA.

Herringe, R.A., Davis, M.R., 1976. Structural development of gas-liquid mixture flows. J. Fluid Mech. 73, 97–123.

Hussain, A.K.M.F., Reynolds, W.C., 1972. The mechanics of on organized wave in turbulent shear flow. Part 2: Experimental results. J. Fluid Mech. 54, 241–261.
Killen, J.M., 1968. The Surface Characteristics of Self-aerated Flow in Steep Channels. Ph.D. thesis, University of Minnesota, Minneapolis, USA.
Kipphan, H., 1977. Bestimmung von Transportkenngrößen bei Mehrphasenströmungen mit Hilfe der Korrelationsmeßtechnik. (Determination of Transport Parameters in Multiphase Flow with Aid of Correlation Measuring Technique). Chem.-Ing.-Techn. 49, 695–707 (in German).
Kökpinar, M.A., 2004. Flow over a stepped chute with and without macro-roughness elements. Can. J. Civil Eng. 31, 880–891.
Leandro, J., Carvalho, R., Chachereau, Y., Chanson, H., 2012. Estimating void fraction in a hydraulic jump by measurements of pixel intensity. Exp. Fluids 52 (5), 1307–1318 (DOI: 10.1007/s00348-011-1257-1).
Lyn, D.A., Rodi, W., 1994. The flapping shear layer formed by flow separation from the forward corner of a square cylinder. J. Fluid Mech. 267, 353–376.
Mossa, M., 1999. On the oscillating characteristics of hydraulic jumps. J. Hydraul. Res., IAHR 37 (4), 541–558.
Mossa, M., Tolve, U., 1998. Flow visualization in bubbly two-phase hydraulic jump. J. Fluids Eng. ASME 120, 160–165.
Ohtsu, I., Yasuda, Y., 1997. Characteristics of flow conditions on stepped channels. In: Proc. 27th IAHR Biennial Congress, San Francisco, USA, Theme D, pp. 583–588.
Press, H., Teukolsky, S.A., Vetterling, W.T., Flannery, B.P., 2007. Numerical Recipes: The Art of Scientific Computing, third ed. Cambridge University Press, New York.
Rao, N.S.L., Kobus, H.E., 1971. Characteristics of Self-Aerated Free-Surface Flows. Water and Waste Water/Current Research and Practice, 10. Eric Schmidt Verlag, Berlin, Germany.
Spiegel, M.R., 1974. Mathematical Handbook of Formulas and Tables. McGraw-Hill Inc., New York, USA.
Stern, R.M., Gouvea, E.B., Thattai, G., 2007. Polyaural array processing for automatic speech recognition in degraded environments. Interspeech, 926–929.
Telionis, D.P., 1981. Unsteady Viscous Flows. Springer, New York, 408 pages.
Thorwarth, J., 2008. Hydraulisches Verhalten der Treppengerinne mit eingetieften Stufen – Selbstinduzierte Abflussinstationaritäten und Energiedissipation (Hydraulics of Pooled Stepped Spillways – Self-induced Unsteady Flow and Energy Dissipation.) Ph.D. thesis, University of Aachen, Germany (in German).
Thorwarth, J., Koengeter, J., 2006. Physical model test on a stepped chute with pooled steps – investigation of flow resistance and flow instabilities. In: Proc. International Symposium on Hydraulic Structures, Caracas, Venezuela, pp. 477–486.
Toombes, L., 2002. Experimental Study of Air-Water Flow Properties on Low-Gradient Stepped Cascades. Ph.D. thesis, Dept. of Civil Engineering, The University of Queensland, Australia.
Toombes, L., Chanson, H., 2007. Surface waves and roughness in self-aerated supercritical flow. Environ. Fluid Mech. 7 (3), 259–270. http://dx.doi.org/10.1007/s10652-007-9022-y.
Toombes, L., Chanson, H., 2008. Interfacial aeration and bubble count rate distributions in a supercritical flow past a backward-facing step. Int. J. Multiph. Flow 34 (5), 427–436 (doi.org/10.1016/j.ijmultiphaseflow.2008.01.005).
Trahiotis, C., Bernstein, L.R., Stern, R.M., Buell, T.N., 2005. Interaural correlation as a basis of a working model of binaural processing: an introduction. In: Popper, A.N., Fay, R.R. (Eds.), Sound Source Localization. Springer, New York, pp. 238–271.
Wood, I.R. 1985. Air water flows. In: Proc. 21st IAHR Biennial Congress, Melbourne, Australia, Keynote address, pp. 18–29.
Wood, I.R., 1991. Air entrainment in free-surface flows. IAHR Hydraulic Structures Design Manual No. 4, Hydraulic Design Considerations, Balkema Publ., Rotterdam, The Netherlands, 149 pages.